The applicability and challenges of black carbon sensors in dense monitoring networks

J. Tapio Elomaa[1], Krista Luoma[1,2], Sami D. Harni[2], Aki Virkkula[2], Hilkka Timonen[2], and Tuukka Petäjä[1]

[1]Institute for Atmospheric and Earth System research / Physics, Faculty of Science, University of Helsinki, Helsinki, Finland
[2]Atmospheric Composition Research, Finnish Meteorological Institute, Helsinki, Finland

Correspondence to: J. Tapio Elomaa (tapio.elomaa@helsinki.fi)

Abstract. Black Carbon (BC) is a particulate pollutant emitted as a by-product of combustion. BC has an emerging role in air quality monitoring with the current recommendations by the World Health Organization that systematic measurements of BC should be conducted to capture the temporal and spatial variability of BC. To observe this variability, especially in urban areas, a large quantity of sensor-type measurements is required. In this study, four different types of small-scale filter-based BC sensors (AE51, MA200, MA350, and Observair) were used to build a sensor network in Kumpula campus, Helsinki, Finland. Our aim was to test the applicability of the sensors to monitor ambient BC concentrations in field conditions and to study the variation of BC at high resolution. The results were compared to a reference level instrument (MAAP) for validation. During intercomparisons, the sensors had a good correlation with the reference and, after a simple orthogonal regression calibration, were deemed suitable for deployment in the sensor network. During deployment, the sensor network proved to be able to capture small-scale temporal and spatial differences in BC concentrations and showed potential for source-apportionment applications. Changes in temperature (*T*) and relative humidity (*RH*) were observed to induce error in the BC measurements. This error was amplified by the dualspot correction, which was worsening the measurement result under instable conditions of *T* and *RH*. This should be considered when using sensors that apply this correction automatically. The environmental compensation used by the Observair sensors reduced the error from the changing *T* and *RH*. To reduce the effect of changing *T* and *RH*, more robust environmentally controlled boxes should be developed or correction algorithms, such as environmental compensation, should be applied.

1 Introduction

Black carbon (BC) is a typical aerosol particle component in the atmosphere. BC consists of carbonaceous material that efficiently absorbs light at visible wavelengths and therefore appears black. It is emitted to the atmosphere as a by-product of incomplete combustion, such as traffic and biomass combustion. BC has remarkable effects on both climate and air quality (Bond et al., 2013).

BC affects the climate directly by interacting with solar radiation and indirectly via complex aerosol-cloud interactions (Stocker et al., 2013). Due to its absorbing nature, BC has a warming effect on the climate. The warming effect is enhanced if BC is emitted or transported in polar areas, where it speeds up the melting of snow and ice sheets by deposition (Sand et al., 2013; Kang et al., 2020; Räisänen et al., 2022).

From the air quality viewpoint, BC is an air pollutant with adverse health effects. Since BC particles fall typically in the size range of ultrafine particles (diameter < 100 nm), they can be transported into the deepest part in the human respiratory system, from there to the blood circulation system, and eventually end up even in the brain and other vital organs (Janssen et al., 2011; Segersson et al., 2017). In addition, combustion related emissions consist of large concentrations of other fine particles and toxic materials. These have been shown to have more adverse health effects than particulate matter from other sources (Krzyzanowski et al., 2005). BC, as a by-product of combustion, has been shown to be a better indicator of the adverse health effects of atmospheric aerosol particles than the more commonly monitored mass of particles smaller than 2.5 µm in diameter ($PM_{2.5}$) (Janssen et al., 2011). In the long run, inhaled fine aerosol particles can cause cardiovascular and respiratory diseases as well as cancer (Ravindra, 2019; Lequy et al., 2021). Lelieveld et al. (2015) estimated that globally exposure to $PM_{2.5}$ cause 1.9 million premature deaths per year.

In the recent air quality guidelines, WHO recommends starting systematic measurements of BC in urban areas to reduce the uncertainty related to temporal and spatial variability of BC concentrations as well as its health, air quality, and climate impacts (WHO, 2021). Even though of the recommendations to monitor BC, there are yet no limit values regarding BC concentration due to lack of epidemiological exposure studies.

Especially in urban areas, the concentration of BC can vary depending on both anthropogenic and natural factors: e.g., changing traffic rate, local biomass combustion, and weather conditions, orography, or close by buildings that affect the dilution by wind or convection (Helin et al., 2018; Caubel et al., 2019; Luoma et al., 2021b). For example, BC concentrations are halved by moving 30m away from a busy traffic lane (Enroth et al., 2016). Due to these various sources and rather short lifetime (days compared to years with greenhouse gases), BC has a lot of temporal and spatial variation within urban districts and communities (Patrón et al., 2017; Caubel et al., 2019; Luoma et al., 2021b).

To capture and measure the spatial and temporal variability of BC in urban areas, one option is to deploy a high-resolution sensor network (Caubel et al., 2019). This requires a large quantity of affordable but robust sensors that can be deployed outside in ambient conditions. A viable option is to utilize commonly used filter-based methods, such as the Aethalometer (Hansen et al., 1984), that are robust, easy-to-use, and have a high time resolution. In the last decade small-scale versions of have been introduced reducing the cost of the sensors in relation to large monitoring instruments by sacrificing some reliability, sensor lifetime and accuracy (Kamboures et al., 2013; Caubel et al., 2018; Holder et al., 2018). In previous studies a common application for these sensors has been personal BC exposure as a carry-on measurement device (Delgado-Saborit,

2012; Li et al., 2015) or they have been utilized in conjunction with larger monitoring instruments (Kuula et al., 2020; Chakraborty et al., 2023).

The large quantity of sensors inevitably causes technical challenges, for example with maintenance, data acquisition, survivability of the sensors under the changing ambient conditions such as diurnal temperature changes and rain, sensor to sensor variability and internal sensor drift (Petäjä et al., 2021; Zaidan et al., 2023). Before a wide implementation of sensor networks, pilot deployments are needed to identify the challenges of individual sensor operations and sensor networks. Operating a variety of sensors side-by-side in the same network allows assessment of performance characteristics of different models of BC sensors, and to identify the critical qualities of a good small-scale BC sensor.

The aim of this study is to explore the suitability of four distinct types of filter-based small-scale BC sensors (AE51, MA200, MA350, Observair) for mapping the spatio-temporal variation of urban BC concentrations. To ensure the measurement quality, we compared the sensors with a Multi-Angle Absorption Photometer (MAAP) (Petzold and Schönlinner, 2004) in two intercomparison periods at Station for Measuring Ecosystem–Atmosphere Relations III (SMEAR III, Järvi et al., 2009) in Kumpula campus, Helsinki, Southern Finland, from the end of May to start of October 2022. In between the two intercomparisons, the sensors were deployed as a sensor network in the surrounding Kumpula campus area. We characterized the applicability of the different sensor types within the sensor network, and the suitability and challenges regarding their utilization in ambient measurements. Furthermore, we provide preliminary results for the general features of BC concentrations within the Kumpula campus area and its spatio-temporal variation.

2 Methods

2.1 Measurement method

An Aethalometer is a filter-based optical method that is widely used to measure BC concentration due to ease of operation and relatively low cost (Hansen et al., 1984). With this technique, sample air is drawn through a filter material, where aerosol particles collected onto the filter. The attenuation of light through the filter area increases over time due to increased absorption and scattering from the collected particles. The attenuation is described by Eq. 1, where I_0 is the light intensity though a clean filter and I is the light intensity through a loaded filter:

$$ATN = -\ln(I/I_0) \quad (1)$$

The measured variable by the instrument is the attenuation coefficient $b_{ATN(\lambda)}$ [m^{-1}] calculated from the measured attenuation and the operational parameters of the instrument as described in Eq. 2, where A [m^2] is the area of the sample spot, Q [$m^3\ s^{-1}$] is the volumetric flow through the sample spot, Δt [s] is the collection time and λ is the wavelength of the light source.

$$b_{ATN}(\lambda) = \frac{A}{Q}\frac{\Delta ATN(\lambda)}{\Delta t} \quad (2)$$

To determine the BC concentration from the attenuation coefficient, a series of assumptions are necessary, and some corrections need to be applied. The attenuation consists of: (1) absorption from the aerosol particles, (2) enhanced attenuation from multiple scattering by the filter fibers (multiple scattering), (3) enhanced attenuation from scattering of the aerosol particles (aerosol scattering) and (4) the saturation of the filter which causes the attenuation to change non-linearly overtime (loading effect) (Collaud Coen et al., 2010). In a general form the BC calculation can be presented as

$$eBC = \frac{1}{MAC(\lambda)} \cdot \sigma_{\mathrm{ap}}(\lambda) = \frac{1}{MAC(\lambda)} \cdot \frac{f(ATN)b_{ATN}(\lambda) - s(\lambda)\sigma_{\mathrm{sp}}(\lambda)}{C_{\mathrm{ref}}} \quad (3)$$

where $\sigma_{ap}(\lambda)$ [m^{-1}] is the absorption coefficient (1), C_{ref} is the multiple scattering correction factor (2), $s(\lambda)$ is a fraction of the scattering coefficient $\sigma_{sp}(\lambda)$ [m^{-1}] (3), $f(ATN)$ is a loading correction function (4), and $MAC(\lambda)$ [$m^2\,g^{-1}$] is the mass absorption cross section (MAC) (Virkkula et al., 2015). The results are given as equivalent black carbon (*eBC*) denoting the conversion of the absorption coefficient to mass concentration with the use of a specific MAC value (Petzold et al., 2013).

The assumptions are that with 880 nm light source the absorption is only from BC particles minimizing the effect of absorbing organic carbon species (i.e., brown carbon, BrC), which absorb on shorter wavelengths. Hence all optical variables are determined at this wavelength. The multiple scattering factor C_{ref} depends on the filter material and instrument used. Most commonly a constant value is used appropriate for the instrument and filter material. It is to be noted that the C_{ref} value can have a large variability depending on seasons, location, and methodology of determination (Collaud Coen et al., 2010; Backman et al., 2017; Di Biagio et al., 2017; Bernardoni et al., 2021; Luoma et al., 2021a). The aerosol scattering correction requires measurement of the scattering coefficient, which in many cases is not possible due to the lack of instrumentation. Due to this the aerosol scattering correction is often voided as in this study. For the loading correction, a plethora of options are available (Bond et al., 1999; Weingartner et al., 2003; Arnott et al., 2005; Schmid et al., 2006; Kirchstetter and Novakov, 2007; Virkkula et al., 2007; Collaud Coen et al., 2010; Hyvärinen et al., 2013; Drinovec et al., 2015; Luoma et al., 2019; Chakraborty et al., 2023). In this study, the dualspot correction (Drinovec et al., 2015; Chakraborty et al., 2023) was tested. The correction was selected as it is the most recent one, it is widely used with Aethalometer model AE33 and capability of this correction is inbuilt to the design of MA200 and MA350 sensors that were utilized in this campaign (see Sect. 2.2). For the MAC value a constant value is commonly used with the assumption that the measured BC is freshly emitted (Bond and Bergstrom, 2006; Bond et al., 2013; Liu et al., 2020).

2.2 Dualspot correction algorithms

The dualspot correction is a scheme to correct for the loading effect by relating two measurement spots with differing flows. The correction is seen in Eq. 4, where eBC_{NC} is the uncorrected measurement and k is the compensation parameter.

$$eBC = \frac{eBC_{\mathrm{NC}}}{(1 - k \cdot ATN)} \quad (4)$$

The k can be determined numerically from the overall loading of the two filter spots as seen in Eq. 5, where subindices L and H refer to the low and high flow spots, respectively (Drinovec et al., 2015). *FVRF* is the face velocity ratio factor.

$$\frac{Q_{\mathrm{L}}}{Q_{\mathrm{H}}} \cdot FVRF = \frac{ln(1 - k \cdot ATN_{\mathrm{L}})}{ln(1 - k \cdot ATN_{\mathrm{H}})} \quad (5)$$

As the k is very sensitive to errors in sample flow measurements, the additional empirical factor *FVRF* is implemented to reduce the sample flow measurement uncertainty. The *FVRF* is calculated by plotting ATN_L/ATN_H to ATN_H and taking the intercept of a linear fit. The linear fit is done when ATN_H is between ATN_{f1} and ATN_{f2} with example values being 10 and 30 respectively. The lower limit (ATN_{f1}) is set to minimize the effect of particle transients in the fresh filter spot and the upper limit (ATN_{f2}) is set low enough so that the data are not yet affected by the loading effect. This should ensure that at the low loading the *ATN* and flow ratios of the two spots are proportional to each other and therefore the sample flow measurement error can be minimized with the *ATN* measurements.

Due to the determination of the *FVRF* and the k being unstable at low loadings and more accurate at high loadings, the k is additionally weighted according to Eq. 6, where k_w is the weighted k, ATN_{TA} is the tape advance trigger (default 120 at 370 nm) and k_{old} is the k calculated from a previous filter spot i.e. before the tape advance:

$$k_w = \frac{(ATN_{TA} - ATN_H)k_{old} + (ATN_H - ATN_{f2})k}{(ATN_{TA} - ATN_{f2})} \quad (6)$$

All in all, the weighing results in that for most of the time the static k_{old} value is used, and the real time determined k according to Eq. 5 rises in importance at higher loadings and closer to the times when the tape advance is triggered. The final weighted k_w at full loading is equal to the real time determined k. The correction is applied to the high flow spot with the weighted k_w and Eq. 4 real time during the measurements.

The MA200 and MA350 sensors utilize a variation of the dualspot correction (Chakraborty et al., 2023; Mendoza et al., 2024). In this version the k is calculated as seen in Eq. 7 and no weighting is used. The data is corrected with the k_{MA} as seen in Eq. 4.

$$k_{MA} = \frac{eBC_L - eBC_H}{(eBC_L * ATN_H) - (eBC_H * ATN_L)} \quad (7)$$

In this study both versions of the correction were tested.

2.3 Small BC sensors

We used four types of small-scale black carbon sensors and one reference instrument. The sensors were AE51 (2 units), MA200 (1 unit) and MA350 (1 unit) by Aethlabs and Observair (OBS, 4 units) by Distributed Sensing Technologies (DST). As the reference instrument, we used the Multi-Angle Absorption Photometer (MAAP) by Thermo Fischer Scientific (Petzold and Schönlinner, 2004).

The sensor specifications are given in Table 1. All small-scale sensors can be operated with flow rates between 50-200 ml min^{-1}. AE51 and Observair measure with one wavelength at 880 nm while the MA-sensors measure with 5 wavelengths (880 nm, 625 nm, 528 nm, 470 nm, 375 nm). All sensors calculate the *eBC* concentration with the 880 nm wavelength according to the assumption to minimize the effect of *BrC*. The MA-sensors have an inbuilt capability for the dualspot correction and therefore two separate measurement spots and one reference spot. The AE51 and Observair have one measurement spot and one reference spot. The AE51 and Observair sensors were run in pairs for the prospect of the dualspot correction (see Sect. 3.2.). The filter materials were for the AE51 Teflon coated quartz fibers (T60), for the MA- sensors polytetrafluoroethylene (L15 or L85 filter cartridge) and for the Observair the filter material was described as fibrous filter material (Distributed Sensing Technologies, 2023). AE51 and Observair had single-use filters that needed to be replaced regularly, in our case every 4-5 days. The MA-sensors have filter cassettes that automatically change the filter spot after a high loading limit is reached. In our case the filter was set to change when *ATN* was higher than 100 at any wavelength (most likely the lowest wavelength of 375 nm), but the setting can be changed between 1-100. The MA200 filter cassette has 15 spots and the MA350 has 85 spots. The filter sample spot is 7.1 mm^2 for all sensor types and all sensors use the same MAC value of 7.8 $m^2 g^{-1}$ (880 nm). The C_{ref} value for AE51 is 1.6 and for the other sensors 1.3. All sensors have additional measurements of temperature and relative humidity (RH) and the Observair sensors utilize environmental compensation technology to compensate for sharp changes in temperature or RH.

The reference instrument MAAP differs from the Aethalometer by additionally measuring scattering to improve the accuracy of the absorption coefficient and *eBC* result. The flow rate was set to 5 l/min. The instrument measures with only one wavelength at 670 nm. The filter tape is made with glass fiber and the tape advance is automatic. In our case, the filter tape

needs to be changed on average every 6 months. The measurement spot is considerably larger, 2 cm^2 in comparison to the small-scale sensors, which was 7.1 mm^2.

160

Table 1. *The types of black carbon sensors used in this study.*

Parameter	**AE51**	**MA200**	**MA350**	**Observair**	**MAAP**
Flow rate [ml min^{-1}]	50-200	50-150	50-150	50-200	5000
Number of wavelengths	1	5	5	1	1
Measurement interval [s]	1-300	1-300	1-300	2-60	300
Filter material	Teflon coated quartz fiber	Polytetrafluoroethylene	Polytetrafluoroethylene	Fibrous	Glass fiber (GF10)
Filter usage	Single	A cassette with 15 spots	A cassette with 85 spots	Single	Tape ~40 m
Sample spot area [mm^2]	7.1	7.1	7.1	7.1	200
MAC [m^2 g^{-1}] (880 nm)	7.8	7.8	7.8	7.8	6.6
C_{ref}	1.6	1.3	1.3	1.3	Measured
Limit of detection [ng m^{-3}]	± 100	± 30	± 30	± 50	± 50

2.4 Deployment area

The field campaign was conducted at the Kumpula Campus area located approximately 4 km northeast from the center of Helsinki, Finland. Helsinki is the capital of Finland located in the south at the coast of the Gulf of Finland. The metropolitan
165 area consists of four cities with a combined population of 1.2 million people (Statistics Finland: Population, Date accessed 01/12/2023, 2023). The main sources of BC in the region are from road traffic, wood burning, maritime traffic and transboundary air pollution (Helin et al., 2018; Teinilä et al., 2022). In 2022, the air quality in the region was good or satisfactory 90% of the time (Helin et al., 2018; Korhonen et al., 2022; Teinilä et al., 2022).

The Kumpula campus area was selected due to easy access for deployment, maintenance, and upkeep. The area consists of variable surroundings with green space, detached housing zones and a relatively high-capacity road. In addition, there was an active construction site in the area during the measurements. Two intercomparison periods were measured during 26.5. – 6.6.2022 (11 d) and 16.9. – 3.10.2022 (17 d) at the Station for Measuring Ecosystem–Atmosphere Relationships III (SMEAR III, 60°12´N, 24°58´E, 26 m above sea level, (Järvi et al., 2009)). In between the intercomparisons 4.7. – 16.9.2022 (74 d), the sensors were deployed to the locations seen in Fig. 1.

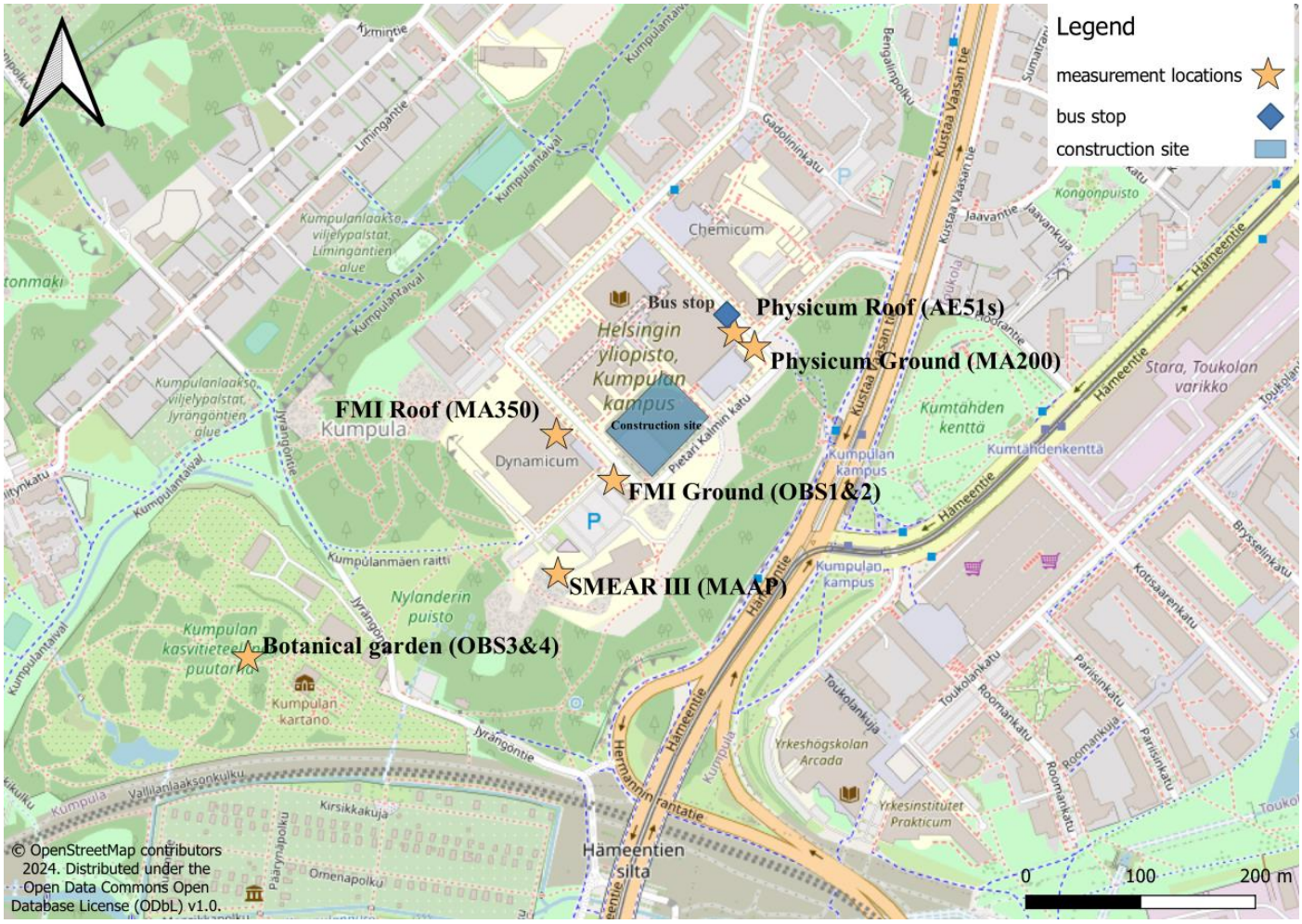

Figure 1. *Map of the deployment locations in the Kumpula campus area.*

Kumpula campus is located on a small hill 26m above sea level. On the Kumpula campus area's southwestern side is the Kumpula botanical garden and park area with trees and vegetation. In the center lies the main university buildings in addition to the Finnish meteorological institute (FMI) with a few four-story apartment blocks. Further north there is a low-density residential area of mainly wooden houses with more park area. On the eastern side there is a road to the city center, Kustaa

Vaasan tie. Kustaa Vaasan tie is used by approximately 38000 – 42000 vehicles per day with around 10% being heavy vehicles (Helsinki city road statistics, Date accessed: 01/02/2024, 2024). Beyond the road lies Toukola residential area with much larger apartment blocks in comparison to the northern side and a small shopping center. The campus area has a bus line going through it with the bus stops marked as small blue squares in Fig 1. Locally, BC is emitted by traffic and wood combustion on the detached housing areas and communal garden.

During the intercomparisons at the SMEAR III, the reference instrument MAAP was used with a pre-impactor removing particles larger than 1 µm in diameter from the sample flow. The inlet was positioned 10 m height from the ground. The small-scale sensors were used without any inlet pre-impactor. The inlets were set up through the SMEAR III station wall at a height of 3 m from the ground.

The deployment locations are described in Table 2. In some locations, two sensors were deployed for redundancy and the possibility of applying the dualspot correction manually. For the dualspot the pairings were run with differing flow rates. The flow rates used during the different phases of the campaign are outlined in Table 3. The closest sources to the locations were a bus stop near the Physicum roof (P_{roof}) and Physicum ground (P_{ground}) locations on a small road. The FMI parking lot in the middle of the FMI roof (F_{roof}), FMI ground (F_{ground}) and the $SMEARIII_{ground}$ locations. The last location, Kumpula botanical garden (BG_{ground}) has minimal traffic. The sensors were flow calibrated during the measurement campaign and the timing and results are outlined in the supplement.

Table 2. *Information of BC sensor deployment locations (height, type, container), deployment lengths and indicated issues related to their operation in this study.*

Location	**P_{roof}**	**P_{ground}**	**F_{roof}**	**F_{ground}**	**BG_{ground}**	**$SMEARIII_{ground}$**
Height	15 m	1.2 m	18 m	1.2 m	1.2 m	10 m
Sensor type and ID	$AE51_{1408}$ $AE51_{1409}$	MA200-0187	MA350-0104	OBS1 (OBS_15) OBS2 (OBS_71)	OBS3 (OBS_74) OBS4 (OBS_37)	MAAP
Container	Inside	B&W Type 3000	B&W Type 3000	Observair's own box	B&W Type 3000	Inside
Deployment length	Full	Full	Partial	Full	Full	Full
Issues	No issues	Temperature dips	Temperature, inlet blocked 22.7 ->, full failure of spot 2 19.7	Overheating due to heater and low battery	Occasionally overheating, missing-> 11-17.8 OBS3, 13-21.7 OBS4, due to low battery	No issues
Notes	Bus stop	Bus stop	Breakdown during deployment	Parking lot	Minimal car traffic in the area	Parking lot

200

Table 3. *Flow rates used during the measurements. Not Available (N.A.) is listed for the sensor data sets, which were not available due to instrument failures*.

	1st Intercomparison		Deployment	2nd Intercomparison
Sensor	26.5 – 31.5.2022 (5d)	1.6 – 6.6.2022 (6d)	4.7. – 16.9.2022 (74 d)	16.9. – 3.10. 2022 (17 d)
$AE51_{1408}$	150 ml min^{-1}	100 ml min^{-1}	100 ml min^{-1}	100 ml min^{-1}
$AE51_{1409}$	150 ml min^{-1}	200 ml min^{-1}	200 ml min^{-1}	200 ml min^{-1}
MA200	150 ml min^{-1}		150 ml min^{-1}	150 ml min^{-1}
MA350	150 ml min^{-1}		150 ml min^{-1}	N.A.
OBS1	145 ml min^{-1}		135 ml min^{-1}	N.A.
OBS2	100 ml min^{-1}		100 ml min^{-1}	N.A.
OBS3	145 ml min^{-1}		145 ml min^{-1}	145 ml min^{-1}
OBS4	100 ml min^{-1}		100 ml min^{-1}	100 ml min^{-1}

2.5 Data analysis

During data processing, data were removed near filter changes. The filter changes were manually identified, and two hours of data were removed starting from the nearest hour before the filter change. This was done for all small-scale sensors.

During the deployment starting from 19.7.2022 the MA350 at F_{roof} had flows significantly lower than the set value. This was most likely due to inlet blockage and the start of a pump failure. Data were removed from this point forward as it was deemed erroneous. The sensor suffered a total pump failure when after it was moved SMEAR III for the 2nd intercomparison (see Sect. 3.2.4).

OBS3&4 located at BG_{ground} had shutdowns due to low battery during the deployment. After the sensor restart the data had erroneous starting spikes. Two hours of data were removed starting from the nearest hour before the restarts. Due to the shutdowns a missing section of OBS3 data are patched with OBS4 data during the deployment. This was done so that the BG_{ground} location has a continuous time series. The sensor-to-sensor variability was deemed low enough as a justification for this process.

In total between 1.5 – 2.9 % of the available data was removed for all sensors except MA350 for which 69.1 % of the data was removed. This section was most of the deployment period. Note that OBS1, OBS2 and MA350 were not tested in intercomparison 2 due to breakage and therefore didn't have available data from that period.

For calibration an F factor was calculated as seen in Eq. 8 using data from the 1st intercomparison. The corresponding sensor data was then multiplied by the reciprocal of this value.

$$F = \frac{eBC_{sensor,mean}}{eBC_{MAAP\_mean}} \quad (8)$$

Python3 was used for most of the data analysis with numpy, scipy, matplotlib, pandas, seaborn and mpl-scatter-density packages (Harris et al., 2020; Hunter, 2007; pandas development team, 2020; Virtanen et al., 2020; Waskom, 2021, https://github.com/astrofrog/mpl-scatter-density, accessed 21.8.2024). For the wind plots R with the openair library was used (Carslaw and Ropkins, 2012).

3. Results and Discussion

3.1 Intercomparison periods

Before and after the deployment, intercomparison measurements were conducted at the SMEAR III to study the differences between the sensor types and the individual units. The sensors were measuring ambient BC concentrations parallel with the reference instrument MAAP. The intercomparison measurements were conducted during 26.5.2022 – 6.6. 2022 (11 d) and 16.9.2022 – 3.10. 2022 (17 d). All the sensors were tested in the 1st intercomparison (AE51 x2, MA200, MA350, OBS x4). During the deployment MA350, OBS1 and OBS2 were damaged and therefore weren't tested in the 2nd intercomparison. Time series of the intercomparisons can be seen in Fig. 2 in 5-minute averages. Correlation of all the sensors in relation to the reference instrument MAAP is seen in Fig. 3 with an orthogonal regression. The values of the orthogonal regression line fit are listed in Table 4. For MA-sensors, spot 1 data are used instead of dualspot corrected data (see sect. 3.1.2).

With 5-minute averaging all sensors showed a good Pearson correlation between 0.78-0.85 during the 1st intercomparison period. Results of AE51 sensors were very comparable with both having an intercept of 42 and slope of 0.84. During this time $AE51_{1408}$ and $AE51_{1409}$ were run with a flow rate of 150 ml min^{-1} between 26.5.2022 – 31.5.2022 (5 d) and 100 ml min^{-1} and 200 ml min^{-1} between 1.6.2022 – 6.6.2022 (6 d) respectively (see Table 3). During the second intercomparison, there were a larger difference, where the $AE51_{1409}$ had a weaker intercept, slope, and correlation of 55.6, 0.70 and 0.92 in

comparison to the respective values for $AE51_{1408}$ of 48.5, 0.78 and 0.94. Both sensors showed improved correlation but weaker slope and intercept.

The MA-series sensors showed similar results where the sensors were comparable to each other with MA200 having intercept, slope, and correlation of 51.5, 1.08 and 0.85 during the 1st intercomparison. The respective values for MA350 were 42.5, 1.13 and 0.83. MA350 did not survive for the 2nd intercomparison. The MA200 showed better performance during the 2nd intercomparison with a correlation of 0.92 and lower intercept of 28.6. The slope reduced to 0.90. The correlation of the MA-series sensors was comparable to the AE51 sensors, but on average the MA-series sensors measured slightly higher concentrations of *eBC*.

From the Observair sensors OBS1 was an older sensor that had been utilized in previous campaigns while OBS 2,3 and 4 were new. The sensors showed very good comparability with correlations in the range of 0.82-0.84 during the 1st intercomparison. The higher flow sensors (OBS1&3) measured slightly higher concentrations than the lower flow sensors (OBS2&4). During the 2nd intercomparison the same pattern was observed, where OBS3 measured slightly higher concentrations compared to OBS4. The reduction of slopes was more drastic during 2nd intercomparison with OBS sensors than AE51s or MA200.

In general, all sensors that were available performed better during the 2nd intercomparison. The correlations were comparable, but there are slight differences on the base *eBC* level between the sensor types. A diurnal cycle can be seen in the intercomparison time series (Fig. 2), where concentrations increase sharply during the mornings and slightly during late evenings. The 1st intercomparison has on average lower concentrations compared to the 2nd intercomparison. This is due to the difference in meteorological conditions and traffic density during these periods. Figure 3. shows the correlation between sensor units and MAAP for *eBC*.

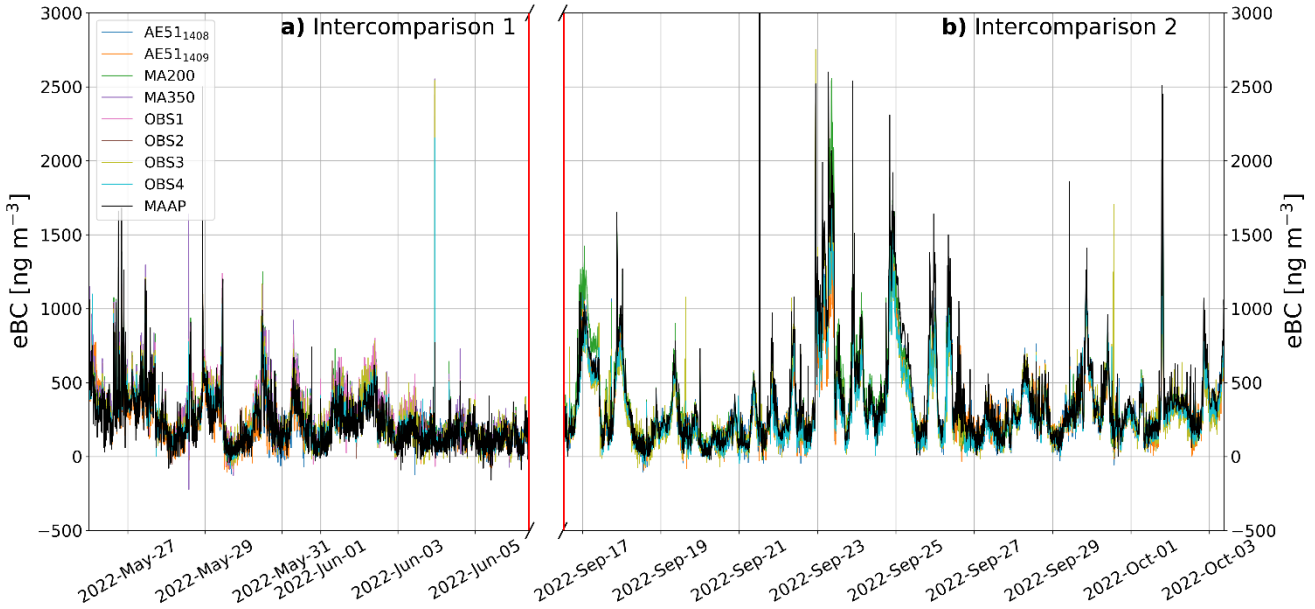

Figure 2. *Timeseries of both intercomparison periods a) 26.5. – 6.6.2022 and b) 16.9. – 3.10.2022. In the figure there is a split x-axis, where the period in between panels (a) and (b) marked with the vertical red lines is approximately 3.5 months. This period was the deployment phase between the intercomparisons. Data points are 5-minute averages.*

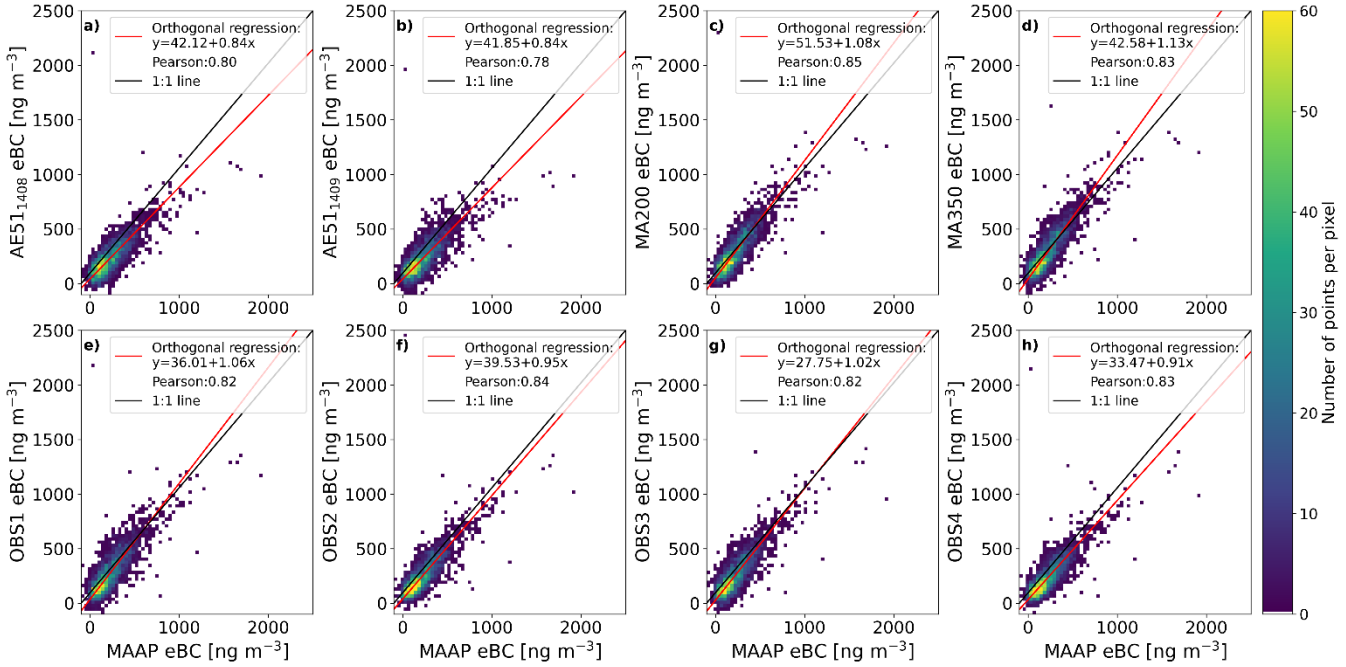

Figure 3. *Scatter density plot of the correlation between the sensors and the reference instrument MAAP. Data are from 1st intercomparisons 26.5. – 6.6.2022 as 5-minute averages.*

Table 4. *Correlation between the sensors and MAAP during the intercomparison measurements (5min, BC). Intercept and slope describe an orthogonal regression line fit. r is pearson correlation. Not Available (N.A.) is listed for the sensor data sets, which were not available due to instrument failures*.

	1st intercomparison 26.5. – 6.6.2022			2nd intercomparison 16.9. – 3.10.2022			Both intercomparisons, if available		
Sensor	Intercept	Slope	r	Intercept	Slope	r	Intercept	Slope	r
$AE51_{1408}$	42.1	0.84	0.80	48.5	0.78	0.94	49.8	0.79	0.92
$AE51_{1409}$	41.9	0.84	0.78	55.6	0.70	0.92	59.1	0.71	0.90
MA200 spot1	51.5	1.08	0.85	28.6	0.90	0.92	53.6	0.90	0.90
MA350 spot1	42.6	1.13	0.83	N.A.	N.A.	N.A.	N.A.	N.A.	N.A.
OBS1	36.0	1.06	0.82	N.A.	N.A.	N.A.	N.A.	N.A.	N.A.
OBS2	39.5	0.95	0.84	N.A.	N.A.	N.A.	N.A.	N.A.	N.A.
OBS3	27.8	1.02	0.82	28.6	0.77	0.91	47.5	0.79	0.88
OBS4	33.5	0.91	0.83	37.9	0.72	0.94	50.6	0.73	0.91

3.1.1 Applicability of the dualspot corrections

Dualspot corrections, that compensate for the loading effect, were tested during the intercomparison periods. The performance of the corrections can be seen in Fig 4, where the sensor data and dualspot corrected data with both methods are compared to the reference instrument MAAP. For MA200 the k_w version of the correction increased the difference to the reference from 21 to 132 ng m^{-3} and with the k_{MA} version from 21 to 48 ng m^{-3}. Most notably the variation of the differences increased in both cases, reducing the precision (seen as larger range of whiskers in Fig. 4) of the measurement. For MA350 the k_w increased the difference from 67 to 145 ng m^{-3} and the k_{MA} decreased the difference from 67 to -22 ng m^{-3}. The precision was reduced, but not as much as for the MA200. For k_{MA} the inverse in the compensation seems to arise from the relative differences of spot 1 and spot 2 and the calculation mechanism. The k value was observed to be highly variable and occasionally beyond reasonable values with both methods. The AE51 and Observair sensors were paired, and the corrections were applied manually by post-processing. For the AE51 the difference improved from -22 to 5 ng m^{-3} with the k_w method and to 8 ng m^{-3} with the k_{MA} method. The precision remained relatively constant with the k_w method and decreased slightly with the k_{MA} method. The correction worked by increasing concentrations at high attenuations and increasing the accuracy of the measurement. For the Observair pairings the corrections increased the difference to the reference for OBS1&2 and for OBS3&4. The k_w correction increased concentrations and the k_{MA} decreased concentrations. For both pairings the corrections reduced the precision of the measurement.

Due to the reduction of the precision in most (4/5) cases, it was decided that the correction is not implemented during the deployment and spot 1 data are used with MA-series sensors. Instead, a simple calibration was used to improve accuracy of the sensors in relation to the reference instrument MAAP. The use of dualspot correction was seen to be highly unstable with both correction methods.

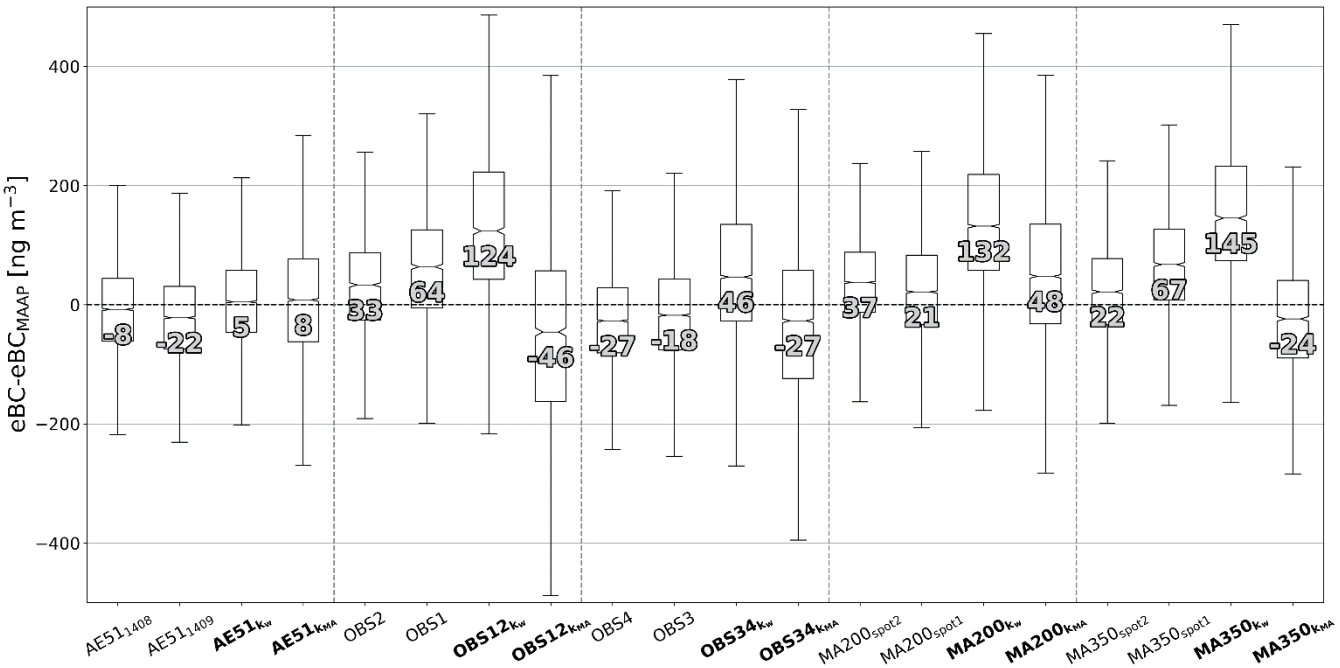

Figure 4. *The effect of the dualspot correction during the intercomparison periods. The dualspot correction is calculated with both correction factors k according to Eqs. 6 and 7. For the MA-sensors the k_{MA} correction is calculated by the instrument. Data are from both intercomparison periods in 5-minute averages. In the plot the middle line shows the median, top of box 75th percentile, bottom of the box 25th percentile and top and bottom whisker the last points within 1.5 times the interquartile range. The values are the medians of the corresponding boxes.*

3.1.2 Sensor calibration

To improve the accuracy and comparability of the sensor types, simple calibrations were applied to the data. Two calibrations were tested: F factor and orthogonal regression line fit. The F factor was calculated according to Eq. 8 and the orthogonal fit calibrations were calculated by applying the sensor respective equations as seen in Fig. 3 and Table 4 to the data. The results of the calibrations can be seen in Fig. 5.

The F factor calibration reduced the spread of the data most aggressively. The medians agreed after the calibration within one standard error of the reference instrument. The orthogonal fit performed near equal to the F factor calibration. For the MA-series the orthogonal calibration overcompensated slightly, but for the Observair sensors this method performed better. After the calibration mean and median values are within ± 5 ng m^{-3} for the Observair sensors, ± 8 ng m^{-3} for the MA-series

and ± 18 ng m^{-3} for the AE51s. All sensor medians were within one standard error of the reference (MAAP) after calibration. Fig. 6 and Table 5 shows the correlation between the data calibrated via the orthogonal fit and MAAP. The new orthogonal line fit intercepts and slopes are within ± 4 ng m^{-3} and ± 0.05 respectively.

The orthogonal regression fit was selected as it considers variation of the sensors and the reference. The whole data set were calibrated according to the orthogonal fit equations determined from the 1st intercomparison. During the analysis this calibration step was observed to be imperative as it reduced the differences between the locations during the deployment phase. Without the calibration differences between locations could have been incorrectly seen as differences in sources, when in fact they were just differences between the instruments.

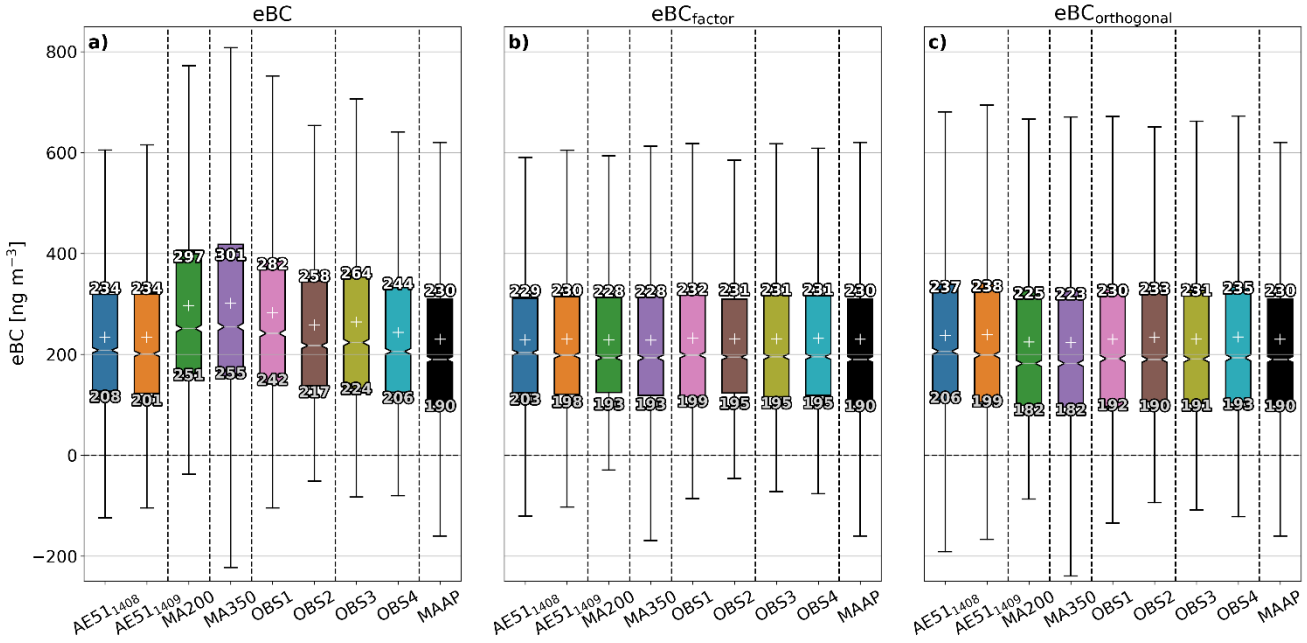

Figure 5. *Calibration methods. Panel a) is data without calibration. Panel b) is data calibrated by an F factor calculated by comparing 1st intercomparison data means. Panel c) is data calibrated with the orthogonal fit equations. In the plot the middle line shows the median, "+" shows mean, top of box 75th percentile, bottom of the box 25th percentile and top and bottom whisker the last points within 1.5 times the interquartile range. The values are the mean (top) and median (bottom).*

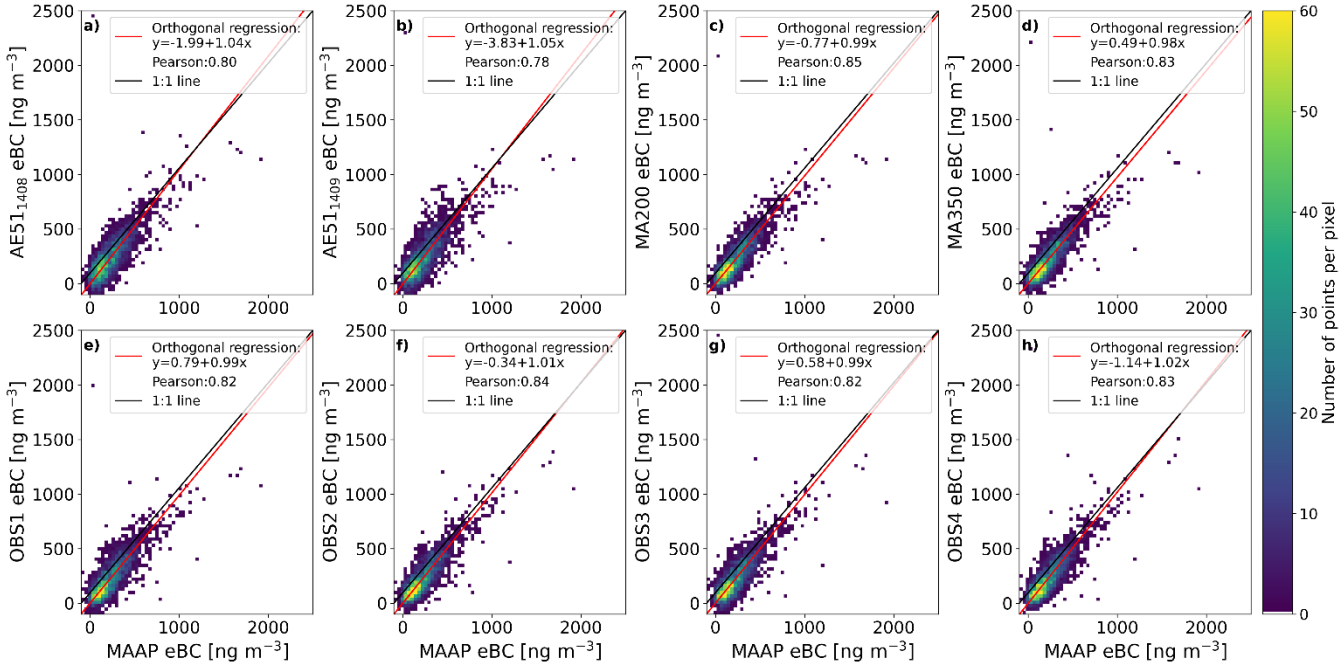

320 **Figure 6**. *Correlation and line fits after calibrating with the orthogonal regression equations seen in Fig. 3.*

Table 5. *Table of the effects of the calibration with the orthogonal regression.*

	1st Intercomparison 26.5-6.6.2022			1st Intercomparison 1 26.5-6.6.2022 after calibration		
Sensor	Intercept	Slope	r	Intercept	Slope	r
AE51$_{1408}$	42.1	0.84	0.80	-1.99	1.04	0.80
AE51$_{1409}$	41.9	0.84	0.78	-3.83	1.05	0.78
MA200 spot1	51.5	1.08	0.85	-0.77	0.99	0.85
MA350 spot1	42.6	1.13	0.83	0.49	0.98	0.83
OBS1	36.0	1.06	0.82	0.79	0.99	0.82
OBS2	39.5	0.95	0.84	-0.34	1.01	0.84
OBS3	27.8	1.02	0.82	0.58	0.99	0.82
OBS4	33.5	0.91	0.83	-1.14	1.02	0.83

3.2 Deployment period

3.2.1 General features of BC in Kumpula

The two-week period is marked in Fig. 7, and comparison between the locations during this period can be seen in the left panel of Fig. 8. The F_{roof} and F_{ground} locations had the lowest concentrations and the highest concentrations of *eBC* were measured at P_{roof} and $P_{ground,}$ respectively. At P_{roof} and P_{ground} multiple short-term high-concentration peaks were observed possibly caused by the proximity of the bus stop. The bus stop has approximately 160 buses stopping on it per day with the peak during the day having 9 to 12 buses per hour. BG_{ground} showed similar median concentration to the P_{roof} and P_{ground} locations, but without the local source peaks at the P_{roof} and P_{ground}. At $SMEARIII_{ground,}$ we observed slightly higher concentrations than at the closest site F_{ground} but lower than the P_{roof} and P_{ground} locations. The local source peaks for MAAP at $SMEARIII_{ground}$ were in between the magnitudes of the respective F_{roof} and F_{ground} to P_{roof} and P_{ground} values. The construction site was not observed to be a major source of BC as the sensors F_{roof} and F_{ground} closest to the cite measured the lowest concentrations. The large variation in data at P_{ground} and F_{roof} (MA200 and MA350, respectively) are due to temperature effects affecting the measurement results (see Sect. 3.2.4).

Minimal vertical difference in the eBC concentration was observed between the P_{roof} and P_{ground} locations. Their median values were within one standard error. Similarly, at F_{roof} and $F_{ground,}$ respectively, minimal vertical difference was observed.

In the right panel of Fig. 8, when considering the whole deployment period, two distinct areas could be identified. The locations closer to the Kustaa Vaasa road of P_{roof} and P_{ground} and the further away backgrounds of $F_{ground,}$ $SMEARIII_{ground}$ and BG_{ground}. The difference between the areas is perhaps traffic proximity due to the Kustaa Vaasa road and bus traffic past the P_{roof} and P_{ground} locations. This causes P_{roof} and P_{ground} to measure approximately 50 ng m^{-3} higher concentrations. The difference is relatively negligible as the instrument precisions are in the same magnitudes and the ambient conditions are challenging for the sensors.

The overall concentrations were lower than previous studies with the Kumpula cite overall being an urban cite. Luoma et al. (2021b) reported annual means of 510 to 530 ng m^{-3} at urban background cites. Helin et al. (2018) reported mean concentrations of 1690 ± 1520 ng m^{-3} at urban cites during wintertime. The lower concentrations are expected as this study is limited to the summertime where traffic rates and wood burning is lower.

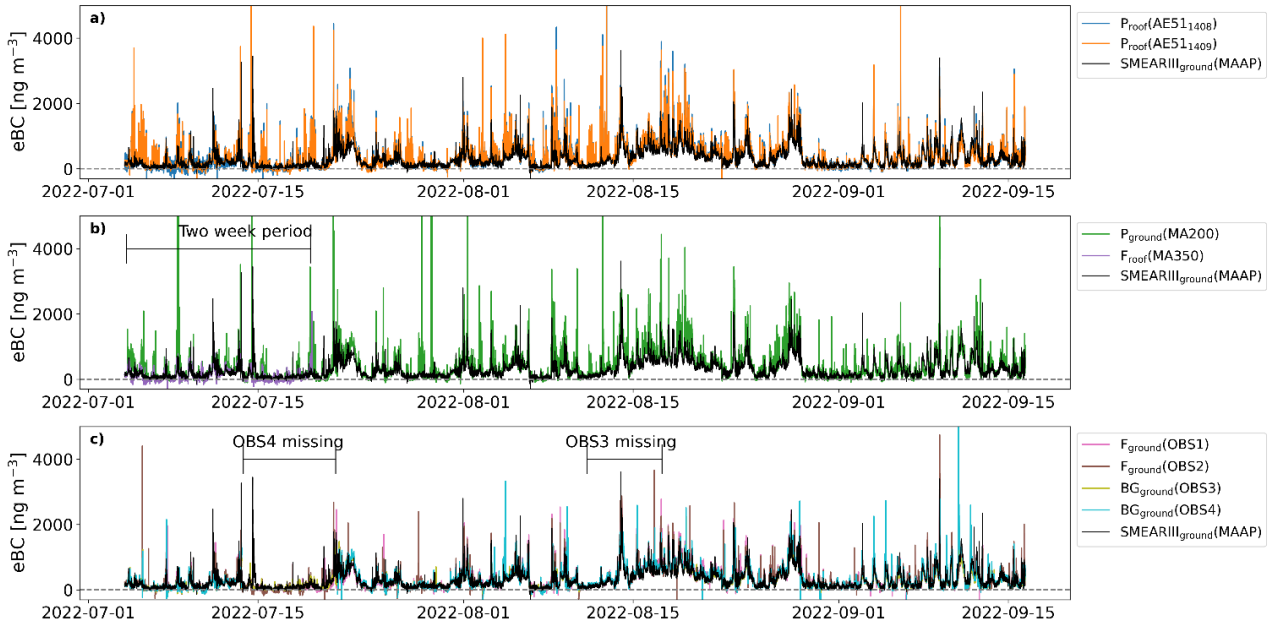

Figure 7. Timeseries of eBC for the deployment period.

Sources of the BC were studied with a wind rose analysis shown in Fig. 9. The wind roses for different locations mostly tell a similar story: highest *eBC* concentrations were measured with low wind speeds especially blowing from the east, when the *eBC* was transported to the campus area from the busy road (Kustaa Vaasan tie). The low wind speeds were also tied to the evening times with the accumulation of pollutants due to the more stable atmosphere.

The effect of the nearby construction site was not clearly visible in the data. Only at the P_{ground} and P_{roof} locations there were some increased concentrations from the direction of the construction site (south-west). For $SMEARIII_{ground}$ or F_{ground}, the direction of the construction site (north-east) did not stand out. At $SMEARIII_{ground}$, increased concentrations on higher wind speeds from west observed, which is probably caused by a single pollution event and was captured due to the higher inlet location. For P_{roof} this direction is also shielded by the building where this location resides.

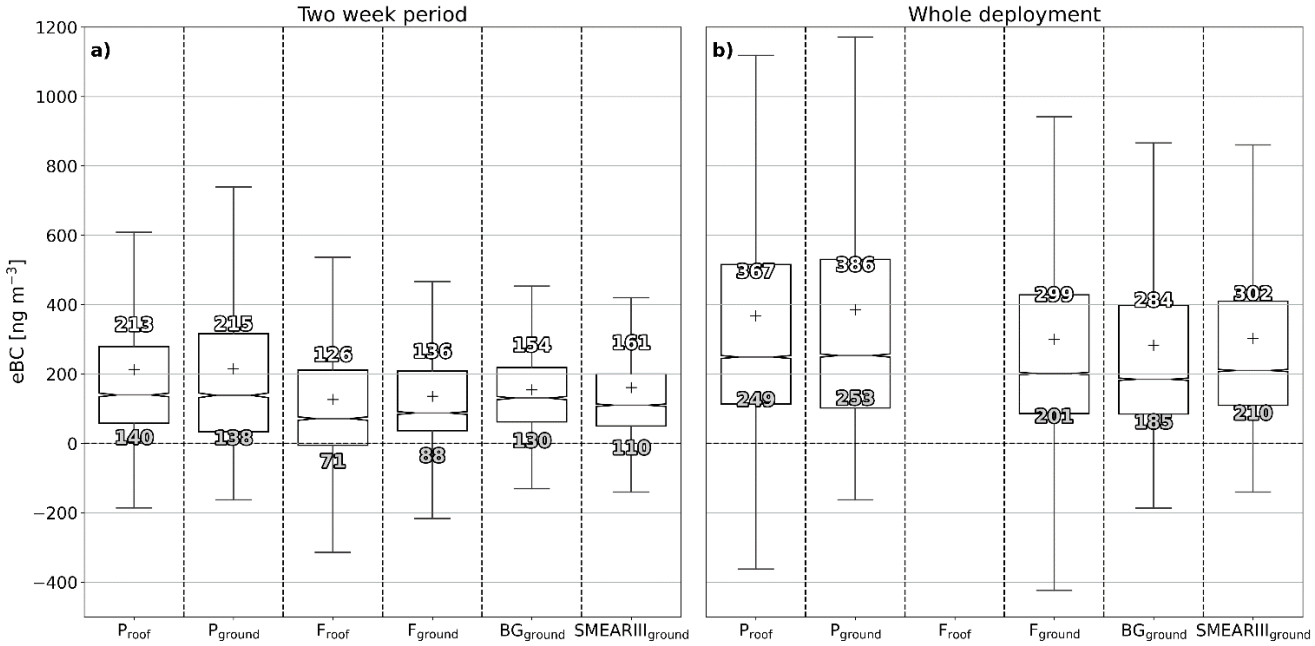

Figure 8. *Boxplot of the whole deployment period. Panel a) data are only from the first 15.5 days (4.7-19.7) of the deployment. Panel b) data are from the whole deployment phase (74 d).*

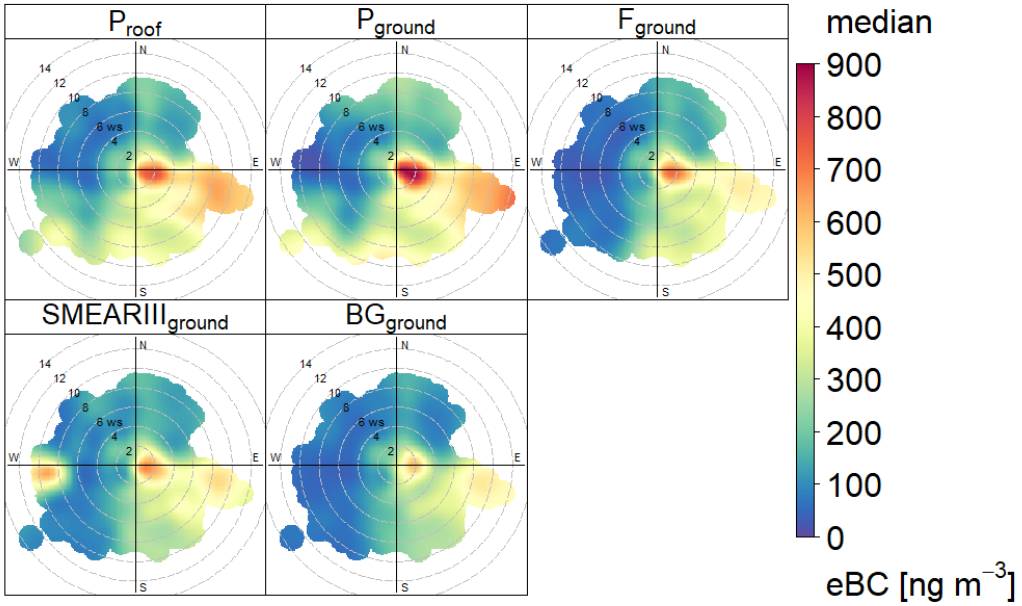

Figure 9. *Wind roses of the deployment phase showing median BC concentration measured with different sensors as function wind speed and direction.*

3.2.2 Weekly features in BC concentration

A daily breakdown can be seen in Fig. 10. There is somewhat surprising variation on day-to-day basis, as no notable differences are expected between weekdays. At all the locations, Mon and Tue had higher concentrations than Wed and Thu, and at most sites the highest concentrations were observed on Fri. Weekend and weekdays do not seem to have a clear difference in the medians to each other, which is differing compared to other studies that observed lower *eBC* concentrations during weekends at traffic and at urban background sites in Helsinki (Helin et al., 2018; Luoma et al., 2021b). Variation might be due to a rather short period (74 d) for such an analysis and the summertime which is a vacation season in Finland.

P_{roof} (AE51) filters were most commonly changed Mon and Fri and F_{ground} and BG_{ground} (Observairs) Mon-Wed with only exception Friday 19.8. With the single filter instruments the significant loading effects should be considered as a pattern of data collection behavior could implicate false patterns of *eBC* in the daily variability. However, a rather similar day-to-day pattern is observed at all the different sites, even at $SMEARIII_{ground}$ and P_{ground}, where the filter was changed automatically at random periods. Therefore, we can conclude that the weekday variation seen in the *eBC* concentrations was not remarkably influenced by the filter changing cycles.

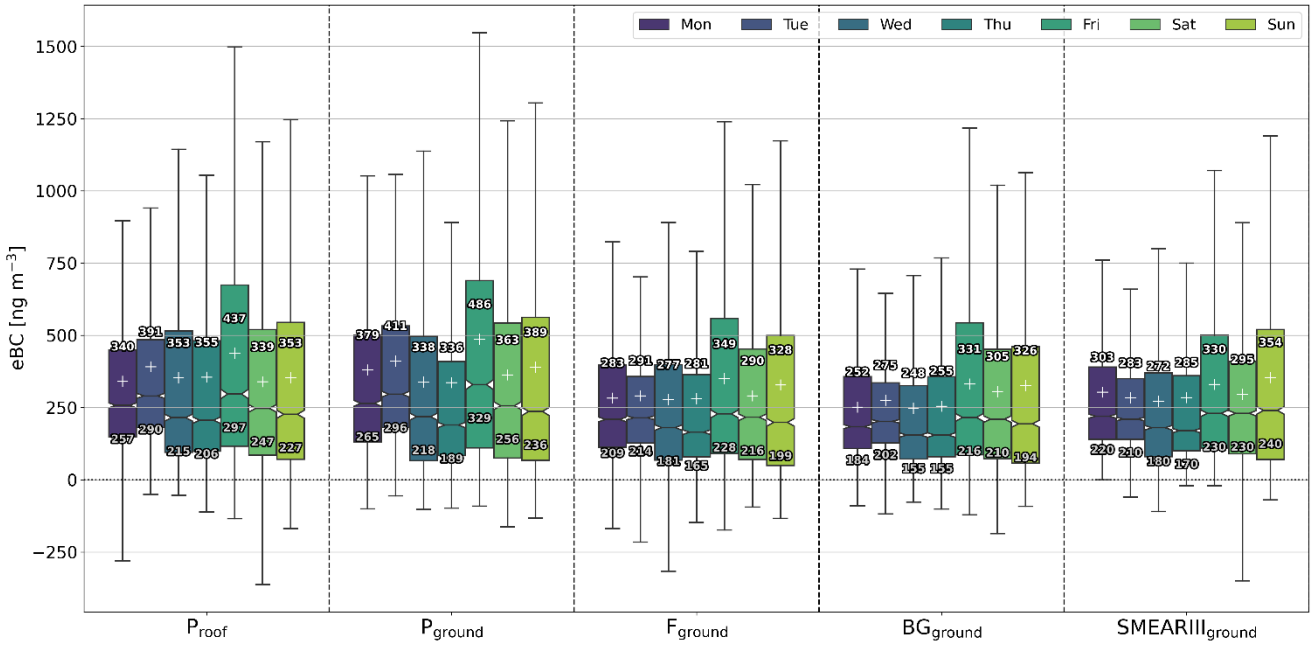

Figure 10. *Daily eBC concentrations for different sensors. In the boxplot every sensor has 7 boxes going left to right as Mon-Sun (indicated with different colors).*

3.2.3 Hourly variation of BC concentrations

An hourly variation of *eBC* can be seen in Fig. 11, which shows a rather similar diurnal pattern at all the locations. The *eBC* concentrations sharply rose during the mornings due to morning traffic. The highest concentrations were reached between 9-10 after which the concentrations decreased due to smaller traffic rates and dilution by the convective boundary layer. Another rise in concentration was observed late in the evening around 21-23. This increase was much less compared to the morning peak. The increased levels during the evenings are probably caused by accumulation of pollutants in a more stable atmosphere. Also, local wood combustion emissions, for example, evening activities at the close by community garden, can increase the *eBC* levels. Similar diurnal patterns have been observed by previous studies during the warm period at traffic and urban background sites (Sahu et al., 2011; Backman et al., 2012; Luoma et al., 2021b).

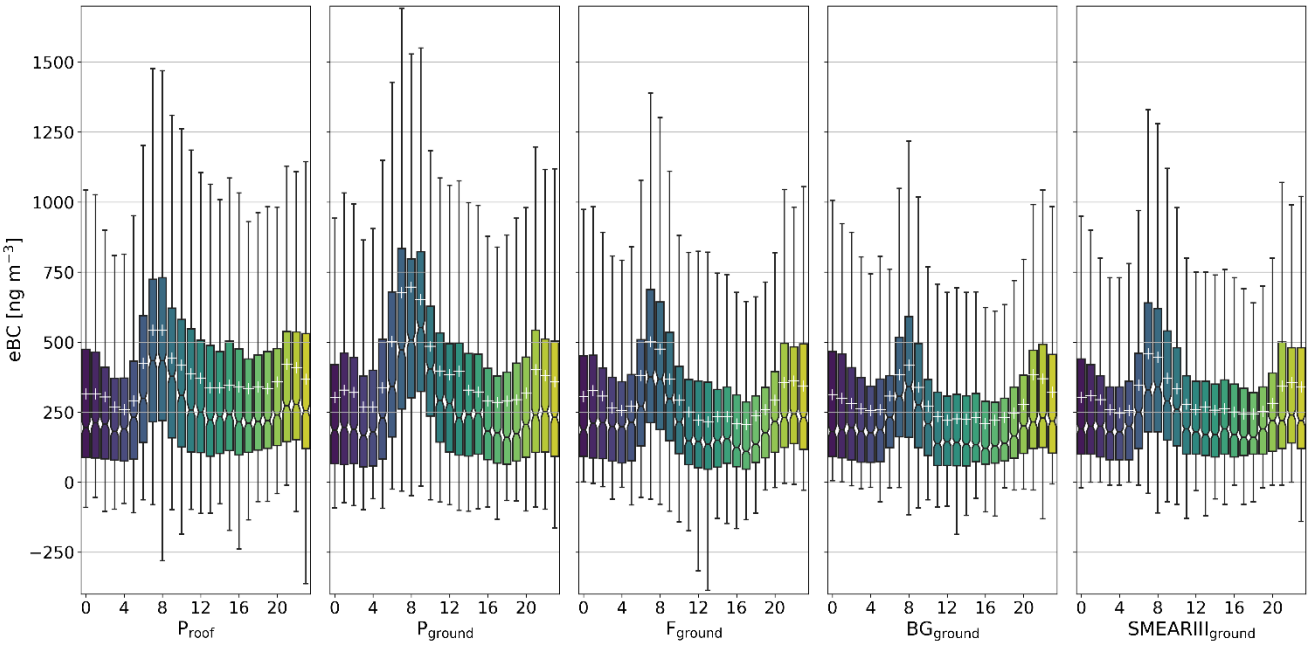

Figure 11. *Hourly variation of eBC concentrations. In the boxplot every sensor has 24 boxes going from 00-23 where the box describes the hour of the day.*

3.2.4 Sensor overheating artifacts

During the measurements overheating of sensors was observed in all locations utilizing the weatherproof boxes (P_{ground}, F_{roof}, F_{ground}, BG_{ground}). This was due to the increase of ambient temperature after sunrise and in some locations direct sunlight heating the black weatherproof boxes.

With the MA-series sensors (MA200, MA350) the change of the temperature and RH caused clearly erroneous data as seen in Figs. 12 and 13. Previous studies have shown that sharp changes in temperature and RH can cause positive or negative

spikes in the measurement of filter-based optical methods (Caubel et al., 2018; Düsing et al., 2019). The reason for this artifact is considered to be mostly influenced by the detector, LED properties and other electronics affected by the temperature change and sorption and desorption of the filter fibers due to changing RH. The largest error in the measurement is when the temperature change was the fastest, around 9-11 in the morning. The dualspot correction was observed to amplify the measurement error of the individual spots.

For the Observair sensors (F_{ground} and BG_{ground}) the influence of overheating was negligible when compared to $SMEARIII_{ground}$, due to the automatic environmental compensation algorithm used in the sensors described in Caubel et al. (2018).

The large overall change in temperature most likely caused a strain on the pumps reducing the lifetime of the sensors. This may have contributed to the failure of the MA350 sensor pump during deployment. With AE51, at the P_{roof}, no problems related to temperature and RH were observed due to the deployment location being inside in a controlled laboratory space, but similar behavior could be expected if these sensors are deployed in ambient conditions.

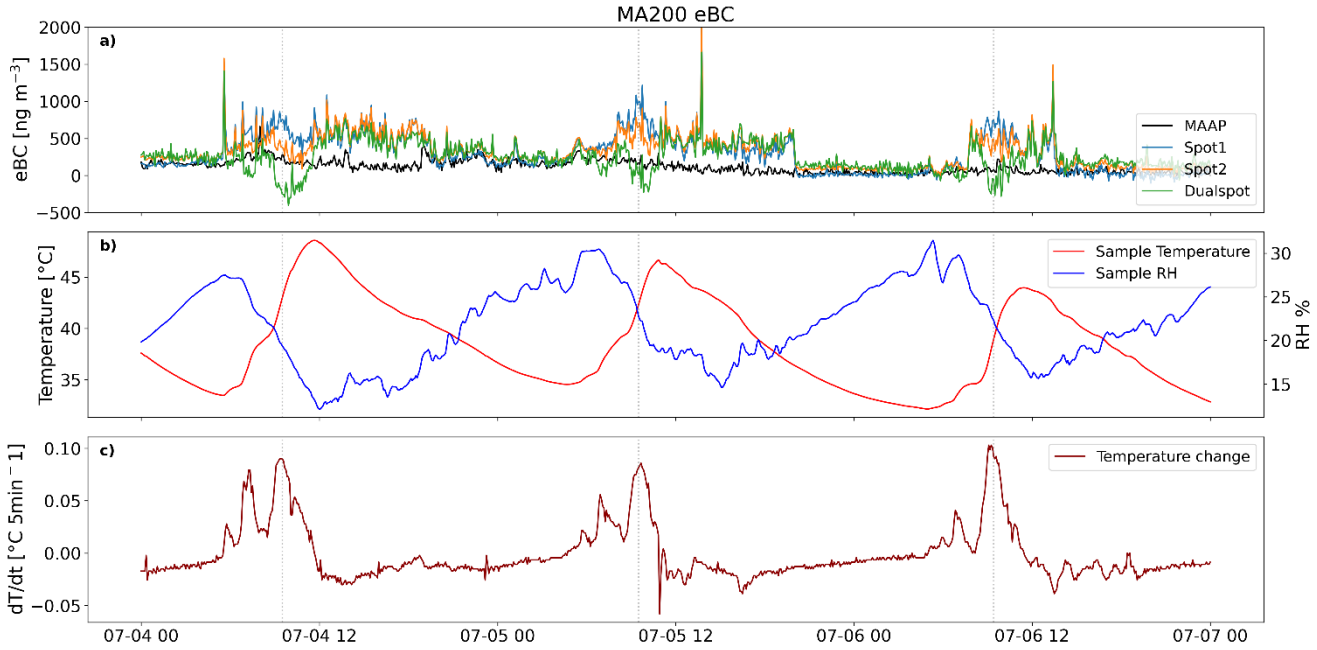

Figure 12. *MA350 temperature/RH artifact. Panels are; a) time series of eBC, b) temperature (°C) and relative humidity (%), and c) the temperature change in (°C 5 min^{-1}).*

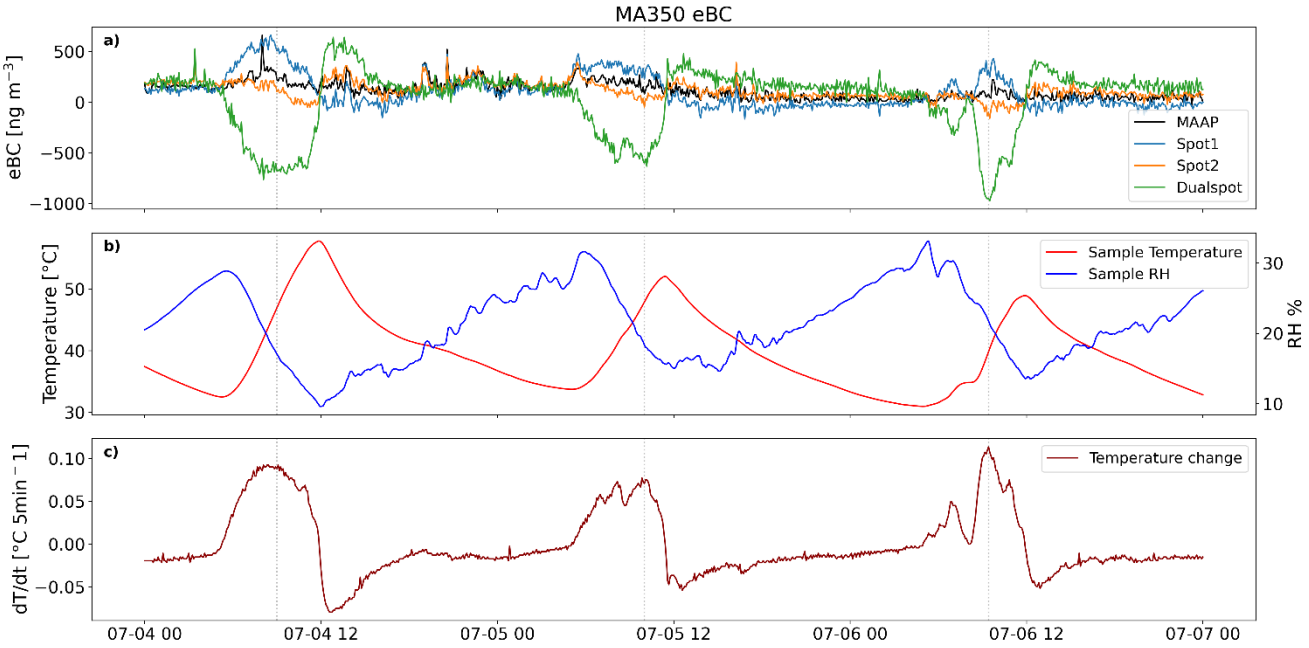

Figure 13. *MA350 temperature/RH artifact. Panels are; a) time series of eBC, b) temperature (°C) and relative humidity (%), and c) the temperature change in (°C 5 min^{-1}).*

4 Conclusions

In this study, four different types *eBC* sensors were used as a sensor network to firstly study variation of *eBC* in urban environment and secondly to study applicability of *eBC* sensors to monitor ambient BC concentrations in real conditions. The results were compared to reference level instrument (MAAP) results to validate the results.

Due to their small size enabling easy installation to existing structures (like sheds or roofs) and affordability the sensors were observed to be well suited to building a sensor network at densely populated urban area. The BC measurements have been conducted since 1970s and thus the used measurement techniques are relatively mature and well known, which helps in the data interpretation significantly. However, still in the field study, several issues were observed. The performance of the dualspot correction should be evaluated before field campaigns for small scale sensors that have the capability for this correction. Due to the small size and much lower flow rates the sensors show significant instability in the determination of the correction parameter *k* with the available methods. In this study during the intercomparison measurements with the dualspot corrections were unstable in temperature and RH controlled environment. During deployment measurements changes in temperature caused additional errors in the measurements of the individual spots which were amplified by the dualspot correction. This effect is especially important with sensors like the MA200 and MA350, which by default give the measurement result as the dualspot corrected data.

Temperature changes significantly affected the measurements and provided a challenge in the deployment of the sensor network. Development of robust enclosures or deployment in locations that have stable or controlled temperature is needed. Alternatively, the environmental compensation used by the Observair sensors was seen to reduce the effect of temperature changes. Unfortunately, the Observair sensors are not being produced as of the end of 2023. Therefore, a suggestion is made that the environmental compensation utilized by the Observair and outlined in Caubel et al. (2018) could be applied as a measurement method to the data via post-processing or implemented to other sensors by manufacturers as a solution to the temperature artifacts. Please note that in the publication Caubel et al. (2018) the name Aerosol Black Carbon Detector (ABCD) is used, which is the academic prototype of the Observair sensor.

It was observed that a dense sensor network could be utilized in source-apportionment of BC in urban areas. This allows the identification of major sources of combustion-based particles or areas and times where the particles are especially prevalent. This information can be used in the urban planning, emission regulations, policy making and emission mitigation for such areas to reduce adverse impacts of BC.

Code availability

Gitlab: https://version.helsinki.fi/elomaata/UAQ2-0

Data availability

Gitlab: https://version.helsinki.fi/elomaata/UAQ2-0

Author contributions

TE did the data analysis and main part of the writing with the help by KL. TE and SH were the main responsible people to build the sensor network and keep it running. All the authors contributed to the planning of the study, interpreting the data, and commenting the manuscript. HT and TP supervised the work and organized the funding.

Competing interests

At least one of the (co-)authors is a member of the editorial board of Aerosol Research.

Acknowledgements

Financial support from Urban Air Quality 2.0 project funded by Technology Industries of Finland Centennial Foundation, H2020 project RI-URBANS (Grant agreement No 101036245), the Academy of Finland via the project Black and Brown Carbon in the Atmosphere and the Cryosphere (BBrCAC) (decision nr. 341271) and Academy of Finland Flagship funding (grant no. 337552, 337549) are gratefully acknowledged

A1. Supplemental material

The sensor flow rates were calibrated before the measurements (on 25.5.) with a Alicat Scientific M-series mass flow meter. The calibration was done manually according to the operating manuals for the AE51s and Observairs and the automatic flow calibration program was used for the MA-series sensors. For OBS1 the flow calibration was ±2 ml min^{-1} and for the other AE51 and OBS sensors ±1 ml min^{-1}. The MA-sensors passed the automatic calibration program. OBS1 and 2 flows were checked after the 1st intercomparison. MA350 was flow calibrated on 9.8. All OBS flows were calibrated on 19.8 and results were within ±1 ml min^{-1}. On 30.8 all sensors were flow calibrated. AE51s were within ±1 ml min^{-1} and OBSs were within ±2 ml min-1. MA200 flow calibration failed, and the flow given by the instrument in relation to the flow meter was +4 ml min^{-1}. Also, during the calibration $AE51_{1408}$ couldn't reach the maximum flow of the pump of 250 ml min^{-1} therefore showing fatigue and deterioration of the pump. The results of flow calibrations are collected to Table A1.

Table A1. *Flow calibrations during the measurements*

Sensor	25.5	6.6	9.8	19.8	30.8
$AE51_{1408}$	±1 ml min^{-1}				±1 ml min^{-1}, couldn't reach max 250 ml min^{-1}
$AE51_{1409}$	±1 ml min^{-1}				±1 ml min^{-1}
MA200	passed				Failed, +4 ml min^{-1}
MA350	passed		passed, was blocked before from 22.7., irregularities from 19.7.	blocked after data loading, tube was loose fixed 30.8.	Tube fixed no flow adjustments
OBS1	±2 ml min^{-1}	checked		±1 ml min^{-1}	±2 ml min^{-1}
OBS2	±1 ml min^{-1}	checked		±1 ml min^{-1}	±2 ml min^{-1}
OBS3	±1 ml min^{-1}			±1 ml min^{-1}	±2 ml min^{-1}
OBS4	±1 ml min^{-1}			±1 ml min^{-1}	±2 ml min^{-1}

References

Arnott, W. P., Hamasha, K., Moosmüller, H., Sheridan, P. J., and Ogren, J. A.: Towards Aerosol Light-Absorption Measurements with a 7-Wavelength Aethalometer: Evaluation with a Photoacoustic Instrument and 3-Wavelength Nephelometer, Aerosol Science and Technology, 39, 17–29, https://doi.org/10.1080/027868290901972, 2005.

Backman, J., Rizzo, L. V., Hakala, J., Nieminen, T., Manninen, H. E., Morais, F., Aalto, P. P., Siivola, E., Carbone, S., Hillamo, R., Artaxo, P., Virkkula, A., Petäjä, T., and Kulmala, M.: On the diurnal cycle of urban aerosols, black carbon and the occurrence of new particle formation events in springtime São Paulo, Brazil, Atmos Chem Phys, 12, https://doi.org/10.5194/acp-12-11733-2012, 2012.

Backman, J., Schmeisser, L., Virkkula, A., Ogren, J. A., Asmi, E., Starkweather, S., Sharma, S., Eleftheriadis, K., Uttal, T., Jefferson, A., Bergin, M., Makshtas, A., Tunved, P., and Fiebig, M.: On Aethalometer measurement uncertainties and an instrument correction factor for the Arctic, Atmos Meas Tech, 10, 5039–5062, https://doi.org/10.5194/amt-10-5039-2017, 2017.

Bernardoni, V., Ferrero, L., Bolzacchini, E., Forello, A. C., Gregorič, A., Massabò, D., Močnik, G., Prati, P., Rigler, M., Santagostini, L., Soldan, F., Valentini, S., Valli, G., and Vecchi, R.: Determination of Aethalometer multiple-scattering enhancement parameters and impact on source apportionment during the winter 2017/18 EMEP/ACTRIS/COLOSSAL campaign in Milan, Atmos Meas Tech, 14, 2919–2940, https://doi.org/10.5194/amt-14-2919-2021, 2021.

Di Biagio, C., Formenti, P., Cazaunau, M., Pangui, E., Marchand, N., and Doussin, J.-F.: Aethalometer multiple scattering correction C_ref for mineral dust aerosols, Atmos Meas Tech, 10, 2923–2939, https://doi.org/10.5194/amt-10-2923-2017, 2017.

Bond, T. C. and Bergstrom, R. W.: Light Absorption by Carbonaceous Particles: An Investigative Review, Aerosol Science and Technology, 40, 27–67, https://doi.org/10.1080/02786820500421521, 2006.

Bond, T. C., Anderson, T. L., and Campbell, D.: Calibration and Intercomparison of Filter-Based Measurements of Visible Light Absorption by Aerosols, Aerosol Science and Technology, 30, 582–600, https://doi.org/10.1080/027868299304435, 1999.

Bond, T. C., Doherty, S. J., Fahey, D. W., Forster, P. M., Berntsen, T., DeAngelo, B. J., Flanner, M. G., Ghan, S., Kärcher, B., Koch, D., Kinne, S., Kondo, Y., Quinn, P. K., Sarofim, M. C., Schultz, M. G., Schulz, M., Venkataraman, C., Zhang, H., Zhang, S., Bellouin, N., Guttikunda, S. K., Hopke, P. K., Jacobson, M. Z., Kaiser, J. W., Klimont, Z., Lohmann, U., Schwarz, J. P., Shindell, D., Storelvmo, T., Warren, S. G., and Zender, C. S.: Bounding the role of black carbon in the climate system: A scientific assessment, Journal of Geophysical Research: Atmospheres, 118, 5380–5552, https://doi.org/https://doi.org/10.1002/jgrd.50171, 2013.

Carslaw, D. C. and Ropkins, K.: Openair - An r package for air quality data analysis, Environmental Modelling and Software, 27–28, https://doi.org/10.1016/j.envsoft.2011.09.008, 2012.

Caubel, J. J., Cados, T. E., and Kirchstetter, T. W.: A new black carbon sensor for dense air quality monitoring networks, Sensors (Switzerland), 18, https://doi.org/10.3390/s18030738, 2018.

Caubel, J. J., Cados, T. E., Preble, C. V., and Kirchstetter, T. W.: A Distributed Network of 100 Black Carbon Sensors for 100 Days of Air Quality Monitoring in West Oakland, California, Environ Sci Technol, 53, https://doi.org/10.1021/acs.est.9b00282, 2019.

Chakraborty, M., Giang, A., and Zimmerman, N.: Performance evaluation of portable dual-spot micro-aethalometers for source identification of black carbon aerosols: Application to wildfire smoke and traffic emissions in the Pacific Northwest, Atmos Meas Tech, 16, https://doi.org/10.5194/amt-16-2333-2023, 2023.

Collaud Coen, M., Weingartner, E., Apituley, A., Ceburnis, D., Fierz-Schmidhauser, R., Flentje, H., Henzing, J. S., Jennings, S. G., Moerman, M., Petzold, A., Schmid, O., and Baltensperger, U.: Minimizing light absorption measurement artifacts of the Aethalometer: evaluation of five correction algorithms, Atmos Meas Tech, 3, 457–474, https://doi.org/10.5194/amt-3-457-2010, 2010.

Delgado-Saborit, J. M.: Use of real-time sensors to characterise human exposures to combustion related pollutants, Journal of Environmental Monitoring, 14, https://doi.org/10.1039/c2em10996d, 2012.

Distributed Sensing Technologies: Observair Operating Manual, https://www.dstech.io/_files/ugd/18a7e0_86bdb3ebd54a49aaaa64e075e1e69604.pdf, April 2023.

Drinovec, L., Močnik, G., Zotter, P., Prévôt, A. S. H., Ruckstuhl, C., Coz, E., Rupakheti, M., Sciare, J., Müller, T., Wiedensohler, A., and Hansen, A. D. A.: The "dual-spot" Aethalometer: an improved measurement of aerosol black carbon with real-time loading compensation, Atmos Meas Tech, 8, 1965–1979, https://doi.org/10.5194/amt-8-1965-2015, 2015.

Düsing, S., Wehner, B., Müller, T., Stöcker, A., and Wiedensohler, A.: The effect of rapid relative humidity changes on fast filter-based aerosol-particle light-absorption measurements: uncertainties and correction schemes, Atmos Meas Tech, 12, 5879–5895, https://doi.org/10.5194/amt-12-5879-2019, 2019.

Enroth, J., Saarikoski, S., Niemi, J., Kousa, A., Ježek, I., Močnik, G., Carbone, S., Kuuluvainen, H., Rönkkö, T., Hillamo, R., and Pirjola, L.: Chemical and physical characterization of traffic particles in four different highway environments in the Helsinki metropolitan area, Atmos Chem Phys, 16, https://doi.org/10.5194/acp-16-5497-2016, 2016.

Hansen, A. D. A., Rosen, H., and Novakov, T.: The aethalometer — An instrument for the real-time measurement of optical absorption by aerosol particles, Science of The Total Environment, 36, 191–196, https://doi.org/https://doi.org/10.1016/0048-9697(84)90265-1, 1984.

Harris, C. R., Millman, K. J., van der Walt, S. J., Gommers, R., Virtanen, P., Cournapeau, D., Wieser, E., Taylor, J., Berg, S., Smith, N. J., Kern, R., Picus, M., Hoyer, S., van Kerkwijk, M. H., Brett, M., Haldane, A., del Río, J. F., Wiebe, M., Peterson, P., Gérard-Marchant, P., Sheppard, K., Reddy, T., Weckesser, W., Abbasi, H., Gohlke, C., and Oliphant, T. E.: Array programming with NumPy, https://doi.org/10.1038/s41586-020-2649-2, 2020.

Helin, A., Niemi, J. V., Virkkula, A., Pirjola, L., Teinilä, K., Backman, J., Aurela, M., Saarikoski, S., Rönkkö, T., Asmi, E., and Timonen, H.: Characteristics and source apportionment of black carbon in the Helsinki metropolitan area, Finland, Atmos Environ, 190, https://doi.org/10.1016/j.atmosenv.2018.07.022, 2018.

Holder, A., Seay, B., Brashear, A., Yelverton, T., Blair, J., and Blair, S.: Evaluation of a multi-wavelength black carbon (BC) sensor, Clean Air Soc. Australia and New ZealandLidcomeA, 770, 2018.

Hunter, J. D.: Matplotlib: A 2D graphics environment, Comput Sci Eng, 9, https://doi.org/10.1109/MCSE.2007.55, 2007.

Hyvärinen, A.-P., Vakkari, V., Laakso, L., Hooda, R. K., Sharma, V. P., Panwar, T. S., Beukes, J. P., van Zyl, P. G., Josipovic, M., Garland, R. M., Andreae, M. O., Pöschl, U., and Petzold, A.: Correction for a measurement artifact of the Multi-Angle Absorption Photometer (MAAP) at high black carbon mass concentration levels, Atmos Meas Tech, 6, 81–90, https://doi.org/10.5194/amt-6-81-2013, 2013.

Janssen, N. A. H., Hoek, G., Simic-Lawson, M., Fischer, P., van Bree, L., Brink, H. Ten, Keuken, M., Atkinson, R. W., Ross Anderson, H., Brunekreef, B., and Cassee, F. R.: Black carbon as an additional indicator of the adverse health effects of airborne particles compared with pm10 and pm2.5, https://doi.org/10.1289/ehp.1003369, 2011.

Järvi, L., Hannuniemi, H., Hussein, T., Junninen, H., Aalto, P., Keronen, P., Kulmala, M., Keronen, P., Hillamo, R., Mäkelä, T., Siivola, E., and Vesala, T.: The urban measurement station SMEAR III: Continuous monitoring of air pollution and surface-atmosphere interactions in Helsinki, Finland, Boreal Environment Research, 14, 1797–2469, 2009.

Kamboures, M. A., Hu, S., Yu, Y., Sandoval, J., Rieger, P., Huang, S. M., Zhang, S., Dzhema, I., Huo, D., Ayala, A., and Chang, M. C. O.: Black carbon emissions in gasoline vehicle exhaust: A measurement and instrument comparison, J Air Waste Manage Assoc, 63, https://doi.org/10.1080/10962247.2013.787130, 2013.

Kang, S., Zhang, Y., Qian, Y., and Wang, H.: A review of black carbon in snow and ice and its impact on the cryosphere, https://doi.org/10.1016/j.earscirev.2020.103346, 2020.

Helsinki city road statistics, Date accessed: 01/02/2024: kartta.hel.fi, last access: 1 February 2024.

Kirchstetter, T. and Novakov, T.: Controlled generation of black carbon particles from a diffusion flame and applications in evaluating black carbon measurement methods, Atmos Environ, 41, 1874–1888, https://doi.org/10.1016/j.atmosenv.2006.10.067, 2007.

Korhonen, S., Loukkola, K., Portin, H., and Niemi, J. V: Ilmanlaatu pääkaupunkiseudulla vuonna 2022, HSY:n julkaisuja 1/2023, 2022.

Krzyzanowski, M., Kuna-Dibbert, B., and Schneider, J.: Health effects of transport-related air pollution, WHO Regional Office Europe, 2005.

Kuula, J., Friman, M., Helin, A., Niemi, J. V., Aurela, M., Timonen, H., and Saarikoski, S.: Utilization of scattering and absorption-based particulate matter sensors in the environment impacted by residential wood combustion, J Aerosol Sci, 150, https://doi.org/10.1016/j.jaerosci.2020.105671, 2020.

Lelieveld, J., Evans, J. S., Fnais, M., Giannadaki, D., and Pozzer, A.: The contribution of outdoor air pollution sources to premature mortality on a global scale, Nature, 525, https://doi.org/10.1038/nature15371, 2015.

Lequy, E., Siemiatycki, J., de Hoogh, K., Vienneau, D., Dupuy, J. F., Garès, V., Hertel, O., Christensen, J. H., Zhivin, S., Goldberg, M., Zins, M., and Jacquemin, B.: Contribution of long-term exposure to outdoor black carbon to the carcinogenicity of air pollution: Evidence regarding risk of cancer in the gazel cohort, Environ Health Perspect, 129, https://doi.org/10.1289/EHP8719, 2021.

Li, B., Lei, X. ning, Xiu, G. li, Gao, C. yuan, Gao, S., and Qian, N. sheng: Personal exposure to black carbon during commuting in peak and off-peak hours in Shanghai, Science of the Total Environment, 524–525, https://doi.org/10.1016/j.scitotenv.2015.03.088, 2015.

Liu, F., Yon, J., Fuentes, A., Lobo, P., Smallwood, G. J., and Corbin, J. C.: Review of recent literature on the light absorption properties of black carbon: Refractive index, mass absorption cross section, and absorption function, Aerosol Science and Technology, 54, 33–51, https://doi.org/10.1080/02786826.2019.1676878, 2020.

Luoma, K., Virkkula, A., Aalto, P., Petäjä, T., and Kulmala, M.: Over a 10-year record of aerosol optical properties at SMEAR II, Atmos Chem Phys, 19, https://doi.org/10.5194/acp-19-11363-2019, 2019.

Luoma, K., Virkkula, A., Aalto, P., Lehtipalo, K., Petäjä, T., and Kulmala, M.: Effects of different correction algorithms on absorption coefficient - A comparison of three optical absorption photometers at a boreal forest site, Atmos Meas Tech, 14, https://doi.org/10.5194/amt-14-6419-2021, 2021a.

Luoma, K., Niemi, J. V., Aurela, M., Lun Fung, P., Helin, A., Hussein, T., Kangas, L., Kousa, A., Rönkkö, T., Timonen, H., Virkkula, A., and Petäjä, T.: Spatiotemporal variation and trends in equivalent black carbon in the Helsinki metropolitan area in Finland, Atmos Chem Phys, 21, https://doi.org/10.5194/acp-21-1173-2021, 2021b.

Mendoza, D. L., Hill, L. D., Blair, J., and Crosman, E. T.: A Long-Term Comparison between the AethLabs MA350 and Aerosol Magee Scientific AE33 Black Carbon Monitors in the Greater Salt Lake City Metropolitan Area, Sensors, 24, https://doi.org/10.3390/s24030965, 2024.

pandas development team: pandas-dev/pandas: Pandas 1.0.3, Zenodo, https://doi.org/10.5281/zenodo.10957263, 2020.

Patrón, D., Lyamani, H., Titos, G., Casquero-Vera, J. A., Cardell, C., Močnik, G., Alados-Arboledas, L., and Olmo, F. J.: Monumental heritage exposure to urban black carbon pollution, Atmos Environ, 170, https://doi.org/10.1016/j.atmosenv.2017.09.030, 2017.

Petäjä, T., Ovaska, A., Fung, P. L., Poutanen, P., Yli-Ojanperä, J., Suikkola, J., Laakso, M., Mäkelä, T., Niemi, J. V., Keskinen, J., Järvinen, A., Kuula, J., Kurppa, M., Hussein, T., Tarkoma, S., Kulmala, M., Karppinen, A., Manninen, H. E., and Timonen, H.: Added Value of Vaisala AQT530 Sensors as a Part of a Sensor Network for Comprehensive Air Quality Monitoring, Front Environ Sci, 9, https://doi.org/10.3389/fenvs.2021.719567, 2021.

Petzold, A. and Schönlinner, M.: Multi-angle absorption photometry—a new method for the measurement of aerosol light absorption and atmospheric black carbon, J Aerosol Sci, 35, 421–441, https://doi.org/https://doi.org/10.1016/j.jaerosci.2003.09.005, 2004.

Petzold, A., Ogren, J. A., Fiebig, M., Laj, P., Li, S.-M., Baltensperger, U., Holzer-Popp, T., Kinne, S., Pappalardo, G., Sugimoto, N., Wehrli, C., Wiedensohler, A., and Zhang, X.-Y.: Recommendations for reporting "black carbon" measurements, Atmos Chem Phys, 13, 8365–8379, https://doi.org/10.5194/acp-13-8365-2013, 2013.

Räisänen, P., Merikanto, J., Makkonen, R., Savolahti, M., Kirkevåg, A., Sand, M., Seland, Ø., and Partanen, A. I.: Mapping the dependence of black carbon radiative forcing on emission region and season, Atmos Chem Phys, 22, https://doi.org/10.5194/acp-22-11579-2022, 2022.

Ravindra, K.: Emission of black carbon from rural households kitchens and assessment of lifetime excess cancer risk in villages of North India, Environ Int, 122, https://doi.org/10.1016/j.envint.2018.11.008, 2019.

Sahu, L. K., Kondo, Y., Miyazaki, Y., Pongkiatkul, P., and Kim Oanh, N. T.: Seasonal and diurnal variations of black carbon and organic carbon aerosols in Bangkok, Journal of Geophysical Research Atmospheres, 116, https://doi.org/10.1029/2010JD015563, 2011.

Sand, M., Berntsen, T. K., Seland, Ø., and Kristjánsson, J. E.: Arctic surface temperature change to emissions of black carbon within Arctic or midlatitudes, Journal of Geophysical Research Atmospheres, 118, https://doi.org/10.1002/jgrd.50613, 2013.

Schmid, O., Artaxo, P., Arnott, W. P., Chand, D., Gatti, L. V, Frank, G. P., Hoffer, A., Schnaiter, M., and Andreae, M. O.: Spectral light absorption by ambient aerosols influenced by biomass burning in the Amazon Basin. I: Comparison and field calibration of absorption measurement techniques, Atmos Chem Phys, 6, 3443–3462, https://doi.org/10.5194/acp-6-3443-2006, 2006.

Segersson, D., Eneroth, K., Gidhagen, L., Johansson, C., Omstedt, G., Nylén, A. E., and Forsberg, B.: Health impact of PM10, PM2.5 and black carbon exposure due to different source sectors in Stockholm, Gothenburg and Umea, Sweden, Int J Environ Res Public Health, 14, https://doi.org/10.3390/ijerph14070742, 2017.

Stocker, T. F., Qin, D., Plattner, G. K., Tignor, M. M. B., Allen, S. K., Boschung, J., Nauels, A., Xia, Y., Bex, V., and Midgley, P. M.: Climate change 2013 the physical science basis: Working Group I contribution to the fifth assessment report of the intergovernmental panel on climate change, https://doi.org/10.1017/CBO9781107415324, 2013.

Teinilä, K., Timonen, H., Aurela, M., Kuula, J., Rönkkö, T., Hellèn, H., Loukkola, K., Kousa, A., Niemi, J. V., and Saarikoski, S.: Characterization of particle sources and comparison of different particle metrics in an urban detached housing area, Finland, Atmos Environ, 272, https://doi.org/10.1016/j.atmosenv.2022.118939, 2022.

Statistics Finland: Population, Date accessed 01/12/2023: https://www.stat.fi/til/vrm_en.html, last access: 1 December 2023.

Virkkula, A., Mäkelä, T., Hillamo, R., Yli-Tuomi, T., Hirsikko, A., Hämeri, K., and Koponen, I. K.: A Simple Procedure for Correcting Loading Effects of Aethalometer Data, J Air Waste Manage Assoc, 57, 1214–1222, https://doi.org/10.3155/1047-3289.57.10.1214, 2007.

Virkkula, A., Chi, X., Ding, A., Shen, Y., Nie, W., Qi, X., Zheng, L., Huang, X., Xie, Y., Wang, J., Petäjä, T., and Kulmala, M.: On the interpretation of the loading correction of the aethalometer, Atmos Meas Tech, 8, 4415–4427, https://doi.org/10.5194/amt-8-4415-2015, 2015.

Virtanen, P., Gommers, R., Oliphant, T. E., Haberland, M., Reddy, T., Cournapeau, D., Burovski, E., Peterson, P., Weckesser, W., Bright, J., van der Walt, S. J., Brett, M., Wilson, J., Millman, K. J., Mayorov, N., Nelson, A. R. J., Jones, E., Kern, R., Larson, E., Carey, C. J., Polat, İ., Feng, Y., Moore, E. W., VanderPlas, J., Laxalde, D., Perktold, J., Cimrman, R., Henriksen, I., Quintero, E. A., Harris, C. R., Archibald, A. M., Ribeiro, A. H., Pedregosa, F., van Mulbregt, P., Vijaykumar, A., Bardelli, A. Pietro, Rothberg, A., Hilboll, A., Kloeckner, A., Scopatz, A., Lee, A., Rokem, A., Woods, C. N., Fulton, C., Masson, C., Häggström, C., Fitzgerald, C., Nicholson, D. A., Hagen, D. R., Pasechnik, D. V., Olivetti, E., Martin, E., Wieser, E., Silva, F., Lenders, F., Wilhelm, F., Young, G., Price, G. A., Ingold, G. L., Allen, G. E., Lee, G. R., Audren, H., Probst, I., Dietrich, J. P., Silterra, J., Webber, J. T., Slavič, J., Nothman, J., Buchner, J., Kulick, J., Schönberger, J. L., de Miranda Cardoso, J. V., Reimer, J., Harrington, J., Rodríguez, J. L. C., Nunez-Iglesias, J., Kuczynski, J., Tritz, K., Thoma, M., Newville, M., Kümmerer, M., Bolingbroke, M., Tartre, M., Pak, M., Smith, N. J., Nowaczyk, N., Shebanov, N., Pavlyk, O., Brodtkorb, P. A., Lee, P., McGibbon, R. T., Feldbauer, R., Lewis, S., Tygier, S., Sievert, S., Vigna, S., Peterson, S., More, S., Pudlik, T., et al.: SciPy 1.0: fundamental algorithms for scientific computing in Python, Nat Methods, 17, https://doi.org/10.1038/s41592-019-0686-2, 2020.

Waskom, M.: seaborn: statistical data visualization, J Open Source Softw, 6, https://doi.org/10.21105/joss.03021, 2021.

Weingartner, E., Saathoff, H., Schnaiter, M., Streit, N., Bitnar, B., and Baltensperger, U.: Absorption of light by soot particles: determination of the absorption coefficient by means of aethalometers, J Aerosol Sci, 34, 1445–1463, https://doi.org/https://doi.org/10.1016/S0021-8502(03)00359-8, 2003.

WHO: WHO global air quality guidelines: particulate matter (PM2. 5 and PM10), ozone, nitrogen dioxide, sulfur dioxide and carbon monoxide, World Health Organization, 2021.

Zaidan, M. A., Motlagh, N. H., Fung, P. L., Khalaf, A. S., Matsumi, Y., Ding, A., Tarkoma, S., Petaja, T., Kulmala, M., and Hussein, T.: Intelligent Air Pollution Sensors Calibration for Extreme Events and Drifts Monitoring, IEEE Trans Industr Inform, 19, https://doi.org/10.1109/TII.2022.3151782, 2023.